

# Combustion of *n*-Butanol, Gasoline, and *n*-Butanol/Gasoline Mixture Droplets

Yuhao Xu and C. Thomas Avedisian\*

Sibley School of Mechanical and Aerospace Engineering, Cornell University, Ithaca, New York 14853, United States

## S Supporting Information

**ABSTRACT:** Fuels derived from biofeedstocks are receiving attention for their potential as additives to conventional petroleum-based transportation fuels. Normal butanol, in particular, can enhance performance compared to ethanol because of its higher energy density. To better understand the combustion dynamics of *n*-butanol in the context of gasoline, experiments are reported here to examine the isolated droplet combustion characteristics of an 87 octane (ethanol-free) gasoline and a mixture of gasoline (0.9, v/v) and *n*-butanol (0.1, v/v, B10), along with *n*-butanol. The experiments are performed in an ambience that minimizes convection and promotes spherical droplet flames. The initial droplet diameters range from 0.52 to 0.63 mm, and the experiments are carried out in room-temperature air at normal atmospheric pressure. Measurements of the evolution of the droplet diameter show that butanol and B10 droplets have burning rates that are almost identical to gasoline, even though other features of the burning process, such as soot formation and the relative position of the droplet and flame, are quite different. With butanol mixed with gasoline, the mixture flames are comparatively closer to the droplet than for gasoline droplets. A scale analysis is developed that expresses the droplet burning rate in terms of temperature-dependent properties. The results support the experimentally observed similarity of burning rates for butanol, gasoline, and their mixtures, even though soot formation is neglected.

## 1. INTRODUCTION

Petroleum-based liquids have been dominate fuels for transportation systems for over a century, and they are projected to be so well into the next century.<sup>1,2</sup> Alternative propulsion and energy concepts (e.g., electric, wind, solar, and geothermal) are not yet at the stage to significantly impact petroleum use<sup>3,4</sup> and meet the transportation and energy needs of modern societies, because none of them match the cost, energy density, and convenience of liquid fuels. Renewable biofuels derived from various biofeedstocks have significant potential to reduce the consumption of petroleum-based fuels, especially as additives to conventional transportation fuels. Ethanol (C<sub>2</sub>H<sub>6</sub>O) is currently widely used for this purpose as an additive to gasoline. However, *n*-butanol (C<sub>4</sub>H<sub>8</sub>O) is also viable as either a neat fuel or an additive.<sup>5–8</sup> When derived from fermentation processes of various microorganisms, butanol (or “biobutanol”) is a renewable fuel.

Normal butanol has several well-known advantages when compared to ethanol, including that *n*-butanol has a higher energy content, greater miscibility with transportation fuels, and lower propensity for water absorption.<sup>9–11</sup> Normal butanol may be blended with gasoline in any concentration, and its comparatively higher energy content would require a lower volumetric concentration compared to a petroleum-derived fuel for similar performance. These features of butanol have motivated renewed interest in its combustion performance.

At one end of complexity to evaluate performance is the in-cylinder environment of an engine. A comparatively large number of studies have examined the combustion of *n*-butanol and blends with gasoline and diesel fuels under realistic engine conditions. Both spark-ignition (SI) and compression-ignition (CI) engines have served as important platforms to examine the

performance of alcohols (including butanol) and blends with gasoline and diesel fuel under realistic conditions (the cited literature is representative of the breadth of previously reported engine studies using butanol, although it is not meant to be a complete listing; other background literature in subsequent discussions is similarly representative).<sup>12–32</sup> Separate but simultaneous injection of butanol and gasoline has also been considered.<sup>33,34</sup>

Engine studies yield useful information about performance under realistic conditions. However, it is an outstanding challenge to predict the in-cylinder environment of a piston engine using detailed numerical modeling (DNM) because of the complex turbulent and swirling motion present. A combustion configuration that can create a more modelable transport configuration is beneficial to understand the combustion physics by its potential to be modeled without any adjustable input parameters. Such configurations for butanol<sup>35</sup> have included flow reactors,<sup>36</sup> shock tubes,<sup>37,38</sup> counterflow flames,<sup>39,40</sup> and jet-stirred reactors.<sup>41</sup> They share the need to prevaporize butanol prior to entering the combustion zone.

Prevaporization of a single-component fuel does not pose significant complications for modeling zero or one-dimensional transport and, thus, to compare predicted combustion properties (e.g., ignition delay time, laminar flame speed, and extinction strain rate) to measured values. Similarly, when the fuel is a multi-component blend, prevaporization prior to ignition simply converts the complex liquid phase to a gas at

Received: January 21, 2015

Revised: March 25, 2015

Published: March 26, 2015

the same composition as the liquid. The modeling challenges are greater, however, for multi-component systems (e.g., surrogate blends) when the flame resides in a multiphase zone that is maintained by evaporation of the liquid. In this case, the gas composition of a multi-component fuel will not be known from the injected composition and the phase equilibrium behavior of the butanol/real fuel blend must be folded into the predictions. This is a more difficult situation to model. A combustion configuration that retains the liquid phase in the combustion environment yet has a modelable (one-dimensional) transport dynamic may be viewed as a more general case to prevaporization and may perhaps better represent the in-cylinder environment of combustion engines powered by condensed phase fuels.

Fuel spray injection is at the heart of almost all liquid-fueled combustion systems. Sprays establish the initial conditions for burning in combustion engines,<sup>2</sup> where the in-cylinder environment can include the presence of droplets.<sup>42–45</sup> However, combustion properties derived from spray flames are difficult to model with the current generation of simulation capabilities without incorporating a significant degree of approximation and sub-model inputs. Considering that the sub-grid scale of a spray is comprised of droplets,<sup>46</sup> only the spherically symmetric droplet burning configuration has been amenable to DNM.<sup>47,48</sup> This configuration has, therefore, been selected to compare the combustion dynamics of butanol to gasoline and a blend of butanol and gasoline. We anticipate that the data obtained will be useful to validate DNM and the complex combustion chemistry inputs to such simulations, as was previously shown for butanol droplet combustion in particular.<sup>47</sup>

The spherically symmetric droplet burning configuration is schematically illustrated in Figure 1. The streamlines of the flow

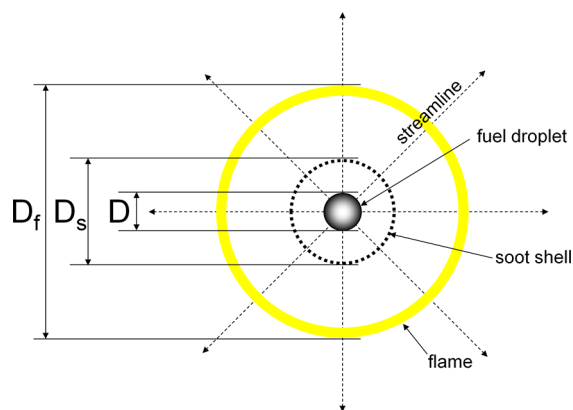


**Figure 1.** Schematic of the spherically symmetric droplet burning configuration.

are purely radial when there is no relative velocity between the droplet and surrounding gas. The flow is created entirely by liquid evaporation. If soot forms, the aggregates will be trapped at a radial distance from the droplet surface where the forces on them balance (i.e., because of thermophoresis and the evaporation-induced velocity<sup>49</sup>).

As far removed from a spray flame as the configuration in Figure 1 may appear, it nonetheless retains many physical processes intrinsic to spray combustion: transient liquid and gas transport, preferential vaporization at the interface, moving boundary effects, variable properties, formation of particulate

matter (i.e., soot), radiative transport, and complex combustion kinetics. A successful DNM for the spherical droplet flame configuration is a building block toward a first-principles simulation of a spray flame, even though the transport is particularly simple.

Several previous studies examined the combustion of butanol droplets, mostly in a strong (buoyant or forced) convecting environment.<sup>50–54</sup> The data reported were useful for showing qualitative trends, although the complexity of the flow environment limited the data to as yet undeveloped DNM capabilities [i.e., that include a two-dimensional axisymmetric laminar (or turbulent) flow field, along with variable properties, time-dependent gas and liquid transport, and multi-step combustion chemistry].

For the simple one-dimensional flow field configuration shown in Figure 1, experiments on butanol and gasoline droplets are scarce<sup>47,55,56</sup> and no studies are known on droplet burning characteristics of butanol/gasoline blends from the perspective of the spherically symmetric configuration. The present paper builds on these prior studies to compare experimentally the combustion dynamics of gasoline, butanol, and a butanol/gasoline mixture in the context of the spherically symmetric droplet flame. The combustion properties include the evolution of droplet ( $D$ ), flame ( $D_f$ ), and soot shell ( $D_s$ ) diameters (except for butanol, which did not produce soot at the operational conditions of the experiments reported here). Considering that it would be most likely for butanol to be blended with gasoline in mixture fractions similar to commercial ethanol/gasoline blends (10% or E10), the particular butanol/gasoline blend selected for study was a mixture of 10% butanol with 90% gasoline, termed “B10”.

There is no basis to *a priori* expect that the combustion properties of butanol would resemble those of gasoline, owing to significant differences between gasoline (e.g., as a highly multi-component, non-oxygenated, and sooting fuel) and butanol (as a single-component, oxygenated, and non-sooting fuel). Nonetheless, the results reported here suggest otherwise in one respect. The data reported were obtained in the standard atmosphere.

## 2. EXPERIMENTAL SECTION

**2.1. Design.** Spherical symmetry was promoted by creating a combustion environment in which the relative velocity between the droplet and surrounding gas is small such that streamlines of the flow will have a linear trajectory in the purely radial direction because they originate from the droplet surface as a result of evaporation. The configuration depicted in Figure 1 would ideally result.

The relevant dynamic scaling to promote spherical symmetry is derived from the Rayleigh and Reynolds numbers,  $Ra = g\beta(T_f - T_\infty)D_f^3/\alpha\eta$  and  $Re = U_{rel}D/\eta$ , respectively, where the characteristic length for buoyancy ( $Ra$ ) is taken as the flame diameter ( $D_f$ , which is related to the droplet diameter) and, for forced convection ( $Re$ ), the initial droplet diameter  $D_0$  is used as the characteristic length. Spherical symmetry is promoted by doing the experiments at low  $g$  (on the order of  $10^{-4}$  of normal gravity on Earth), using small droplets with  $D_0$  between 0.52 and 0.63 mm, and employing a stagnant gas in the experiments. Droplet motion is restricted by anchoring it to very small support structures or fibers.

Low gravity is created by carrying out the experiments in a free fall such that the droplet with its immediate surroundings is burned while it falls. The ambient is room-temperature air at normal atmospheric pressure. The experimental design and procedures are briefly discussed below. Further details are given in refs 55, 57, and 58.

Droplets are deployed at the intersection of two very small [ $14\ \mu\text{m}$  diameter ( $D_{fiber}$ )] SiC fibers crossed at an angle of approximately  $60^\circ$

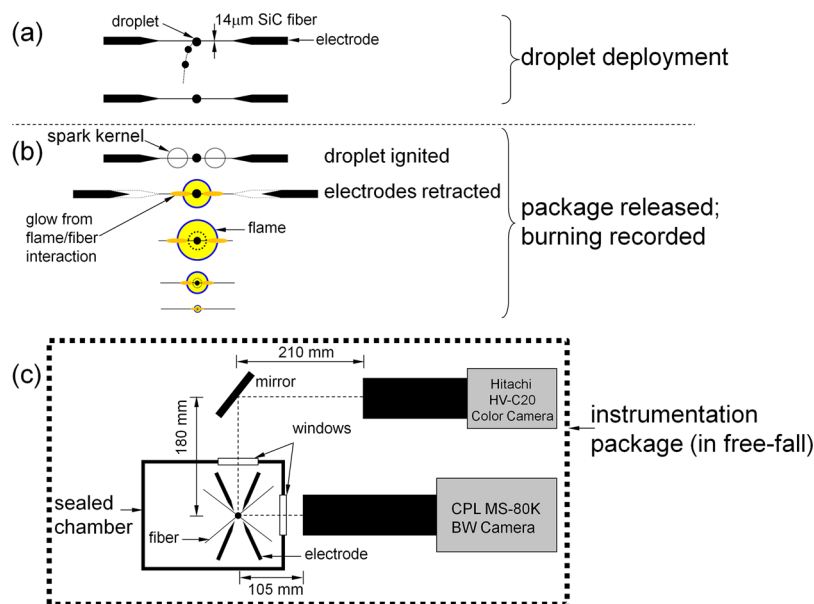


**Figure 2.** Schematic of the experiment: (a) droplet deployment by piezoelectric generation onto SiC fibers, (b) sequence of events for ignition and initiation of low gravity, and (c) arrangement of cameras and droplet for recording the burning process. The hardware in panel c is in free fall during an experiment to minimize the influence of buoyancy.

(this angle is not important, except that it should not restrict visibility of the droplet in perpendicular directions). When the fibers are crossed and the droplet is mounted at the intersection, the droplet will not slide during the burning process. Deployment to the intersection is by generating a droplet from a piezoelectric generator (cf. panels a and b of Figure 2). The hardware for the fiber mount and droplet generator are enclosed in a sealed chamber (Figure 2c) that is charged with room-temperature air. It has previously been shown that the support fiber design described here minimally influences the droplet burning rate.<sup>57,58</sup>

Once deployed, the instrumentation package (Figure 2c) is released into free fall from 7.6 m to provide about 1.2 s of experimental run time. During the fall, the droplet is ignited by spark discharge across two electrode pairs positioned on opposite sides of the droplet to provide some degree of ignition symmetry. The sparks are activated 320 ms after free fall begins, and they are on for 800  $\mu$ s, after which they are rapidly retracted from the combustion zone so as not to greatly influence the thermal field developed around the droplet during its burning history. After each experiment, the chamber is thoroughly flushed with air and then sealed for a new experiment. The time sequences of deployment, release, and ignition are coordinated by a multi-channel digital signal generator (Quantum Composer, QC-9618).

It should be noted that the idealization depicted in Figure 1 is difficult to achieve in practice. Internal liquid circulation may exist because of artifacts of the droplet deployment process<sup>59</sup> that will not be evident from the state of gas-phase symmetry. As a result, the term “spherically symmetric” is used here with regard to the outward appearance of such.

The diagnostic for the experiments is digital videography provided by two cameras that give perpendicular views of the droplet while it burns (cf. Figure 2c). The video images are analyzed (see section 2.2) to obtain quantitative measurements of  $D$ ,  $D_f$ , and  $D_s$ . A black and white (BW) digital camera (Canadian Photonics Laboratories, Inc., MS-80K, 3.9 megapixels (MP)/frame, operated at 200 fps, fitted with an Olympus Zuiko 90 mm  $f/2.0$  lens, an Olympus OM Telescopic Extension Tube 65–116 mm (fixed at 100 mm), and a Vivitar MC 2 $\times$  teleconverter) provides backlit images to observe the droplet and sooting dynamics. Backlighting is provided by a 1 W light-emitting diode (LED) lamp (Black Diamond Equip., Ltd.). A color video camera (Hitachi HV-C20, 0.3 MP/frame, operated at 30 fps, fitted

with a Nikkor 135 mm  $f/2.0$  lens and two Kenko 36 mm extension tubes) records self-illuminated flame images.

**2.2. Data Analysis.** Measurements of  $D$ ,  $D_f$ , and  $D_s$  are extracted from video images using either a computer-based algorithm developed previously<sup>60</sup> or a manual approach using commercial software packages (Image-Pro Plus, version 6.3, for  $D$  and  $D_s$  and CorelDraw 9 for  $D_f$ ). The algorithm identifies the relevant boundaries automatically using a gray-scale threshold to obtain an area-averaged diameter (cf. Figure 3a, which shows a droplet with the droplet boundary

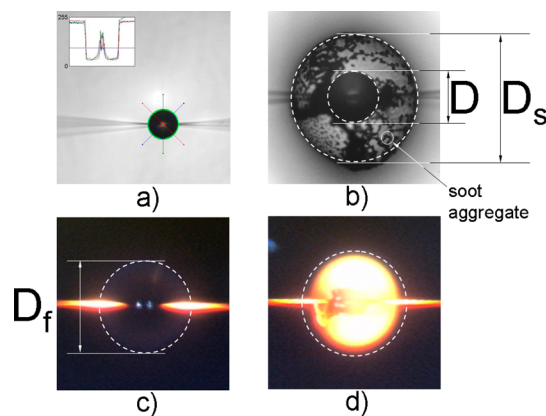


**Figure 3.** Analysis of BW and color images: (a) droplet diameter as determined by a computer algorithm<sup>60</sup> (inset shows a computer-generated color gradient across the droplet boundary), (b)  $D$  and  $D_s$  as determined by manual positioning of the virtual ellipse, (c)  $D_f$  for relatively non-sooting butanol using a virtual ellipse, and (d)  $D_f$  for luminous flame of B10.

indicated by the green circle). For the manual approach, droplet diameters are determined manually by placing a virtual ellipse on the image and positioning it based on personal judgment of the boundary (cf. the dotted boundaries in panels b and c of Figure 3 for  $D$ ,  $D_f$ , and  $D_s$ ). The major ( $H$ ) and minor ( $W$ ) axes of the ellipse are determined from the software, and an equivalent diameter is obtained as  $D = (HW)^{0.5}$ . This approach is always taken for measurements of  $D_f$  and  $D_s$

extractions, where  $D_i$  is defined by the outer boundary of a blue luminous zone (cf. Figure 3d).

**2.3. Chemical Analysis.** The composition of the gasoline used in the present study was determined by gas chromatography/mass spectrometry (GC/MS) consisting of an Agilent 7683 series injector, Agilent 6890N network GC system, and Agilent 5973N mass selective detector. GC analysis was performed with a 30 m capillary DB-5 column (with a column diameter of 0.25 mm and coating thickness of 0.25  $\mu\text{m}$ ). The injection inlet temperature was 250  $^{\circ}\text{C}$ . The oven temperature was held at 40  $^{\circ}\text{C}$  for 2 min, heated at 5  $^{\circ}\text{C}/\text{min}$  to 50  $^{\circ}\text{C}$ , then heated at 25  $^{\circ}\text{C}/\text{min}$  to 150  $^{\circ}\text{C}$ , and held there for 5 min. Helium was used as the carrier gas with a pressure of 9.34 psi, giving an average velocity of 40 cm/s. A 0.2  $\mu\text{L}$  sample was injected with a split ratio of 15:1.

The mass spectrometer is set to detect the mass range of  $m/z$  26–350. The interface and ion source temperatures were 310 and 230  $^{\circ}\text{C}$ , respectively. Data sampling time was carried out from 0 to 13 min in the measurement mode of “scan”.

To identify the chemical species of main peaks in the chromatogram, the mass spectrum of each peak was compared to a National Institute of Standards and Technology (NIST) mass spectral library. The chemical species of each peak was determined manually by matching with the NIST library.

**2.4. Fuel Systems.** Representative fuel properties are listed in Table 1. *n*-Butanol came from Sigma-Aldrich with 99.8% purity, as

**Table 1. Selected Properties of Fuels Examined**

property	gasoline	<i>n</i> -butanol	B10
formula	$\text{C}_{8.26}\text{H}_{15.50}^a$	$\text{C}_4\text{H}_{10}\text{O}$	
stoichiometric coefficient, $\nu^b$	12.135	6.0	
molecular weight, $W$ (g/mol)	114.8	74.12	
boiling point (bp, K) <sup>c</sup>	305.7 (initial bp) 327.3 (10% distilled) 378.7 (50% distilled) 432.8 (90% distilled) 471.6 (final bp)	390.9 <sup>d</sup>	305.4 (initial bp) 331.2 (10% distilled) 375.3 (50% distilled) 430.7 (90% distilled) 467.0 (final bp)
liquid density, $\rho_L$ (kg/m <sup>3</sup> ) <sup>e</sup>	726	805	734
anti-knocking index <sup>f</sup>	87	91.5 <sup>g</sup>	
burning rate, $K$ (mm <sup>2</sup> /s) <sup>h</sup>	0.532	0.512	0.524
flame temperature (K) <sup>i</sup>	2243	2233	

<sup>a</sup>From ref 62. <sup>b</sup>Assuming 1 mole of fuel and products of  $\text{CO}_2$  and  $\text{H}_2\text{O}$ . <sup>c</sup>Boiling points for gasoline and B10 are from ref 68. <sup>d</sup>From ref 66. <sup>e</sup>Measured using a digital density meter (Mettler Toledo DA-100M) at 297.6 K. <sup>f</sup>Anti-knocking index (AKI) = [research octane number (RON) + motor octane number (MON)]/2. <sup>g</sup>From refs 69 and 70. <sup>h</sup>Estimated from Figure 8. <sup>i</sup>From ref 12.

specified by the manufacturer. Because gasoline is known to exhibit some reasonable variations of composition, a fresh supply of 87 octane gasoline was obtained in 2013 for the present study (from a SavOn gas station, Oneida, NY). GC/MS analysis of the gasoline used in the present study (cf. Figure 4) indicates a highly multi-component mixture with a composition that consists of *n*-alkanes, aromatics, branched alkanes, and no oxygenated compounds (e.g., ethanol). Previous studies<sup>47,55</sup> examined the combustion dynamics of an 87 octane-grade gasoline [acquired in 2009 from a local service station (a Mobil dealer in Ithaca, NY)] and *n*-butanol. Those data, along with the new measurements for gasoline, are compared here to data for a gasoline/butanol mixture. The gasoline/butanol mixture was prepared on a volume basis.

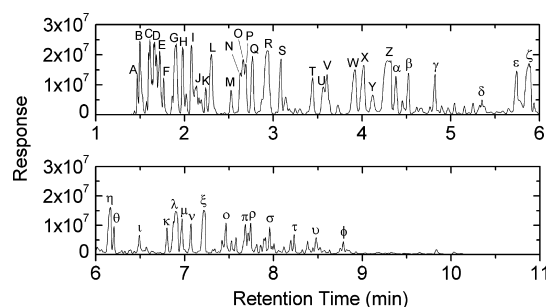


**Figure 4.** GC/MS measurements for the gasoline in this study. The main peaks are as follows: (A) isobutane, (B) butane, (C) 2-methylbutane, (D) pentane, (E) 2-methyl-1-butene, (F) 2,2-dimethylbutane, (G) 2-methylpentane, (H) 3-methylpentane, (I) hexane, (J) 3-methyl-2-pentene, (K) (Z)-3-methyl-2-pentene, (L) methylcyclopentane, (M) 1-methylcyclopentane, (N) benzene, (O) 2-methylhexane, (P) 2,3-dimethylpentane, (Q) 3-methylhexane, (R) iso-octane, (S) heptane, (T) methylcyclohexane, (U) 2,5-dimethylhexane, (V) 2,4-dimethylhexane, (W) 2,3,4-trimethylpentane, (X) 2,3,3-trimethylpentane, (Y) 2,3-dimethylhexane, (Z) toluene, ( $\alpha$ ) 2,4-dimethylheptane, ( $\beta$ ) 2,2,5-trimethylhexane, ( $\gamma$ ) octane, ( $\delta$ ) 2,5-dimethylheptane, ( $\epsilon$ ) ethylbenzene, ( $\zeta$ ) 1,3-dimethylbenzene, ( $\eta$ ) 1,2-dimethylbenzene, ( $\theta$ ) nonane, ( $\iota$ ) (1-methylethyl)benzene, ( $\kappa$ ) propylbenzene, ( $\lambda$ ) 1-ethyl-3-methylbenzene, ( $\mu$ ) 1,2,3-trimethylbenzene, ( $\nu$ ) 1-ethyl-2-methylbenzene, ( $\xi$ ) 1,3,5-trimethylbenzene, ( $\omicron$ ) 1,2,4-trimethylbenzene, ( $\pi$ ) 1-methyl-3-propylbenzene, ( $\rho$ ) 1-methyl-2-(1-methylethyl)benzene, ( $\sigma$ ) 4-ethyl-1,2-dimethylbenzene, ( $\tau$ ) 1,2,3,5-tetramethylbenzene, ( $\upsilon$ ) 2,4-dimethylstyrene, and ( $\phi$ ) naphthalene.

### 3. RESULTS

**3.1. Photographs of Droplet Burning.** Visualizations of the droplet burning history provide qualitative information on the burning process, and they serve as the primary “data” from which quantitative measurements are obtained. The quality of the video images is important for accuracy and precision of the measurements.

Figure 5 shows representative color images of gasoline, B10, and butanol<sup>47</sup> droplets (panels a, b, and c of Figure 5, respectively), while Figure 6 shows backlighted images of these same fuels. The numbers give the times after ignition. The horizontal glows (Figure 5) on either side of the flames are due to interactions between the flame and support fibers.

The flame structures in panels a and b of Figure 5 consist of bright yellow cores because of soot incandescence and much fainter outer blue zones (perhaps because of emission from CH radicals). The butanol flame structure (Figure 5c) is comprised mainly of a relatively dim blue zone, indicating a virtually non-sooting flame in keeping with the atmospheric pressure conditions of the burning environment (at elevated pressures, alcohols can form soot).

Figure 6 shows droplet and soot configurations from backlighted images. The schematic of Figure 1 is qualitatively consistent with the images in panels a and b of Figure 6. Particularly large soot aggregates accumulate later in the burning process and drift outwardly (Figure 6b at 0.5 and 0.6 s). This effect may be due to the stability of the aggregates at the trapped position. Larger aggregates are predicted to be less locked into a radial location, where the forces on them balance, compared to smaller aggregates.<sup>61</sup> The large aggregates will then be more susceptible to small perturbations of the burning process that initiate drifting of the agglomerates away from the droplet.

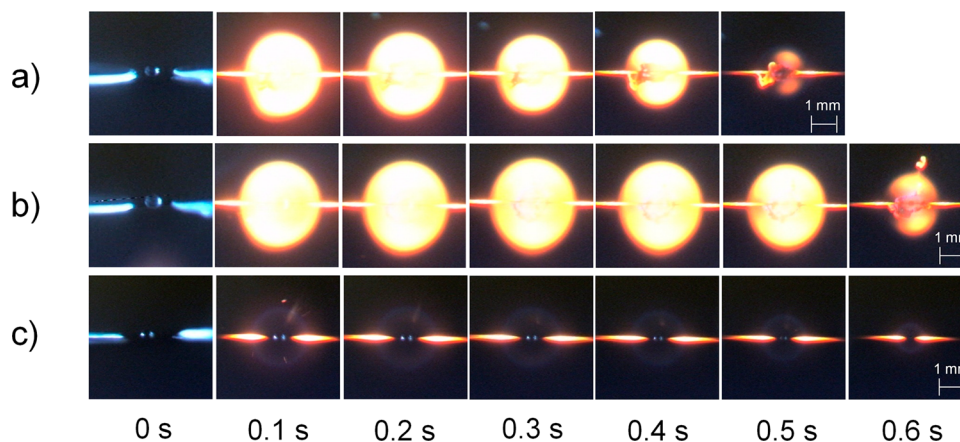


**Figure 5.** Selected color images showing evolutions of spherical droplet flames: (a) gasoline ( $D_o = 0.52$  mm), (b) B10 ( $D_o = 0.61$  mm), and (c) butanol<sup>47</sup> ( $D_o = 0.56$  mm). The scale is indicated in the last image of each sequence.

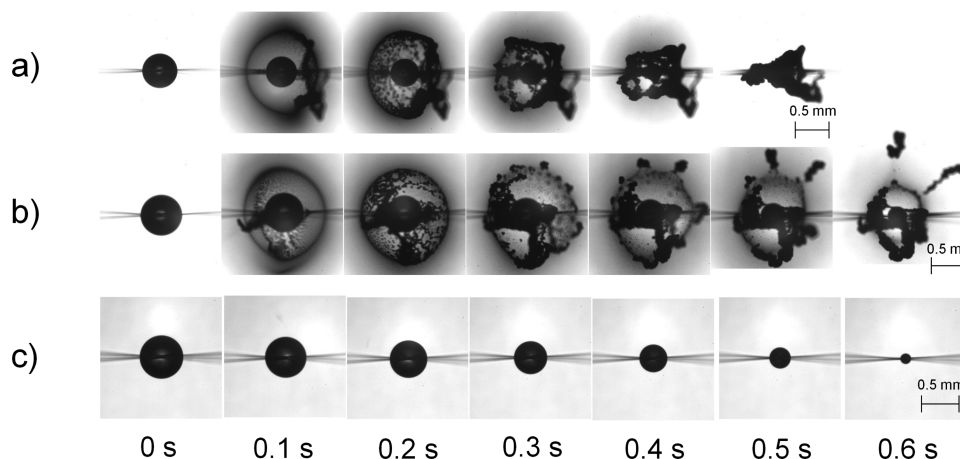


**Figure 6.** Selected backlit BW images showing evolutions of droplet size and soot dynamics: (a) gasoline ( $D_o = 0.52$  mm), (b) B10 ( $D_o = 0.61$  mm), and (c) butanol<sup>47</sup> ( $D_o = 0.56$  mm). The scale is indicated in the last image of each sequence.

Although the fiber diameter is small ( $D_o/D_{\text{fiber}} > 36$  initially), the fiber still exerts some influence on the soot structure, as shown in Figure 6, where aggregates accumulate on the fiber. Nonetheless, the photographs do not show the sort of microconvective effects observed previously in fiber-supported experiments of large droplets<sup>57</sup> that may have been induced by the retraction process of the ignition coils in those experiments.

As the aggregates grow during burning, they can obscure part of the droplet boundary, as shown for gasoline and B10 in panels a and b of Figure 6. The analysis of such images is more problematic and accomplished by the manual approach discussed in section 2.2. The images for the butanol burning sequence in Figure 6c are especially clear and well-suited to the data analysis algorithm previously developed<sup>60</sup> for extracting measurements of  $D$ .

**3.2. Quantitative Data.** Figure 7 shows the measured evolution of droplet diameter for gasoline, butanol,<sup>47</sup> and B10, and Figure 8 presents these data as averages (the data in Figures 7–10 are included in the Supporting Information). The measurements are presented using coordinates from the quasi-steady theory of droplet burning,<sup>62</sup> in which a scaled droplet diameter is  $(D/D_o)^2$  and a scaled time is  $t/(D_o^2)$ . The slope in these coordinates is the burning rate,  $K \equiv |d(D/D_o)^2/d(t/(D_o^2))|$ , which is a measure of the combustion rate of a fuel. It should be independent of time by the quasi-steady theory.

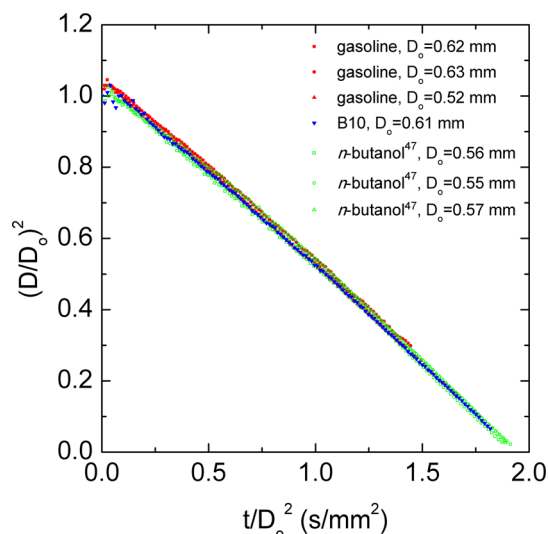


**Figure 7.** Evolution of the droplet diameter from individual experiments for all fuels investigated in this study.

Figure 8 includes data from previous studies,<sup>47,55</sup> which shows the consistency of the present results. Linearizing the measurements in Figure 8 over the range of  $0.2 \leq t/(D_o^2) \leq 1.3$  s/mm<sup>2</sup> gives the burning rates listed in Table 1, which differ

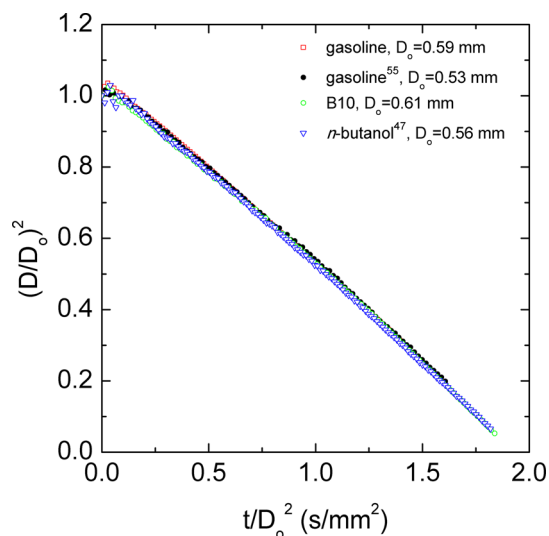


**Figure 8.** Evolution of the average droplet diameter for data in Figure 7.

by about 4%. This difference is well within the uncertainty of the burning rate measurements.

Gasoline is a highly multi-component fuel (Figure 4) consisting of constituents with a range of boiling points, heats of vaporization, and sooting tendencies. As a result, it might be anticipated that a preferential vaporization effect could occur, in which the mixture components are transported to the droplet surface and evaporate in the order of their volatilities.  $K$  would then adjust (and change) during the burning process as one species becomes depleted from the surface, while others (with different properties) are transported there and evaporate. The data in Figures 7 and 8 do not suggest this conjecture because  $K$  shows no evidence of changing during burning. Moreover, the evolution of  $D$  for the “binary” B10 also exhibits a monotonic and essentially linear variation with time. On the other hand, if the evaporation process is very fast and overwhelms transport by mass diffusion, the mixture components will only evaporate when the surface regresses to expose them. The droplet composition then remains frozen during burning. In this event,  $K$  may be considered a sort of compositionally averaged value and an apparent single value of  $K$  would result. This seems to be the case for the data in Figures 7 and 8. A detailed numerical model of droplet combustion<sup>47,48,63</sup> would best reveal the physical mechanism responsible for the trends shown in the data.

The confluence of the droplet diameter data in Figures 7 and 8 is interesting considering that the fuels have different sooting propensities (Figure 6). Soot formation was previously speculated to exert a plethora of physical and chemical effects on burning.<sup>49,64</sup> However, Figures 7 and 8 suggest that soot formation may in fact not have a strong influence on the burning rate for the small droplet sizes examined here because the sooting propensities for gasoline and butanol are vastly different yet their burning rates are virtually identical. This possibility could also explain why a DNM of the configuration of Figure 1 that did not include soot formation achieved high-fidelity predictions of the burning process of *n*-heptane droplets, which formed soot and soot shells.<sup>63</sup>

The relative position of the droplet to the flame,  $D_f/D$ , is shown in Figure 9, which also includes previous results.<sup>55</sup> It is evident that the distance of the flame to the droplet increases

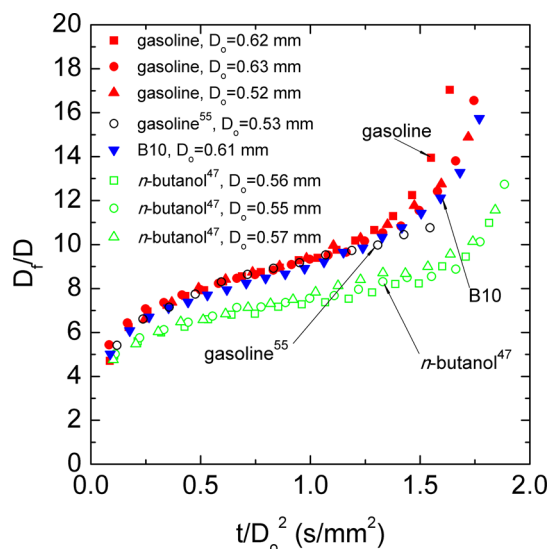


**Figure 9.** Evolution of the flame standoff ratio ( $D_f/D$ ) for the fuels investigated in this study.

with time during burning and that the gasoline used here produces droplet flames that are positioned from the droplet surface at a location consistent with prior work (previous flame images<sup>55</sup> were reanalyzed to produce the data shown in Figure 9). The time dependence of  $D_f/D$  indicates that the burning process is not quasi-steady, because consideration of only the burning rate might otherwise lead one to conclude that it is quasi-steady.

It is seen in Figures 8 and 9 that the droplet burning characteristics for the 87 octane gasoline examined in this study are virtually identical to results from the previously used<sup>55</sup> gasoline sample. These samples were obtained at significantly different periods when it might have been expected that there would be seasonable variations in performance. As shown in Figures 8 and 9, however, this appears not to be the case because the burning rates and relative positions of the flame to the droplet are almost identical.

The trends noted above are explained by a scale analysis similar to one previously carried out.<sup>65</sup> We neglect soot formation and radiation, assume constant properties, and draw on the quasi-steady theory of droplet burning for how the burning rate depends on parameters. From the classical theory of droplet burning,<sup>62</sup> we can write that

$$K_i \sim \frac{k_i/C_{p,i}}{\rho_{L,i}} \quad (1)$$

For unity Lewis number,  $k_i/C_{p,i} = \rho_i D_i$  and noting that<sup>66</sup>

$$\rho_i D_i \sim C_D (M_i T_{f,i})^{1/2} \quad (2)$$

where the flame temperature is used, eqs 1 and 2 combine to give

$$K_i \sim \frac{(M_i T_{f,i})^{1/2}}{\rho_{L,i}} \quad (3)$$

apart from a constant.

Only gasoline and butanol need to be compared because they bound the burning rate of B10, as shown in Figures 7 and 8. Defining  $\Phi_K \equiv K_g/K_b$  and using eq 3, we can write

$$\Phi_K \sim \left( \frac{M_g T_{f,g}}{M_b T_{f,b}} \right)^{1/2} \frac{\rho_{L,b}}{\rho_{L,g}} \quad (4)$$

Using the property values in Table 1 in eq 4 gives  $\Phi_K \sim 1.06$ . For the measured burning rates in Table 1,  $\Phi_K \sim 1.04$ . Considering the approximations involved with this simple scaling, these results are remarkably close, to both each other and unity, which is consistent with the data in Figures 7 and 8. It is interesting that soot formation is neglected in this scaling yet gives results consistent with the experiments. This points to other influences (e.g., gas diffusion and temperature) as potentially being responsible for the similarity of the droplet burning rates. A detailed numerical model of a sooting fuel (*n*-heptane) which neglected soot formation predicted *n*-heptane droplet burning rates that also agreed well with measured values.<sup>63</sup>

For the relative position of the droplet to the flame, a modification of a formulation developed by Aharon and Shaw<sup>67</sup> is used to show that, for gasoline and butanol

$$\Phi_F \equiv \frac{(D_f/D)_g}{(D_f/D)_b} \sim \left( \frac{\rho_{L,g}}{\rho_{L,b}} \right) \left( \frac{K_g}{K_b} \right) \left( \frac{\nu_g}{\nu_b} \right) \left( \frac{W_b}{W_g} \right) \quad (5)$$

Using property values from Table 1, eq 5 gives  $\Phi_F \sim 1.22$  [which is realized at about  $t/(D_o^2) \approx 1.0$  s/mm<sup>2</sup> in Figure 9]. More importantly,  $\Phi_F > 1$ , which is qualitatively consistent with the data in Figure 9 that shows gasoline droplet flames being farther from the droplet surface than butanol droplet flames. These simple developments show the importance of scale analysis to explain the experimental trends and to suggest the physics behind the experimental results.

The soot shell standoff ratio,  $D_s/D$ , is shown in Figure 10. There are no data for butanol because butanol does not

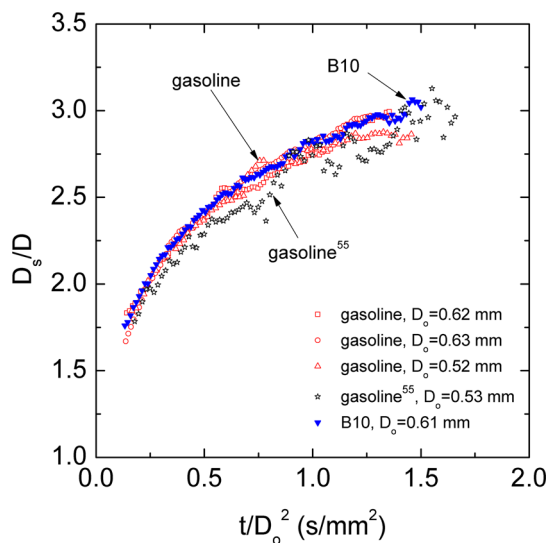


**Figure 10.** Evolution of the soot standoff ratio ( $D_s/D$ ) for the fuels investigated in this study.

produce soot under the conditions examined (cf. Figure 6c). The  $D_s/D$  data for gasoline reported here are consistent with previous results<sup>55</sup> (also shown in Figure 10), which further support the observation noted previously that the two gasoline supplies (the present and earlier<sup>55</sup>) were consistent enough to yield very similar burning characteristics. Also, near the end of

burning, soot aggregates typically agglomerated for gasoline into a self-supported “crust”, so that a freely levitated shell could not be considered as arising from a balance of forces on the aggregates. It is for this reason that the  $D_s/D$  data terminate at about  $t/(D_o^2) \approx 1.5$  s/mm<sup>2</sup>, while Figures 7–9 show data extending to  $t/(D_o^2) \approx 1.75$  s/mm<sup>2</sup> that are not influenced by soot within the viewing field.

As expected and on the basis of Figures 6 and 9, the soot shell clearly resides between the droplet and flame (i.e.,  $D_s/D < D_f/D$ ) because soot will form only on the fuel-rich side of the droplet diffusion flame.  $D_s/D$  also follows the time dependence of  $D_f/D$ : as the flame expands, so too does the soot shell. These measurements are important to provide a more complete picture of the droplet burning process and for their potential to be incorporated in a DNM of droplet burning that would include soot formation (although no predictive capability for soot formation currently exists).

#### 4. CONCLUSION

The droplet combustion characteristics of gasoline, butanol, and a gasoline/butanol mixture are compared for the base case of droplet burning in an environment that promotes spherical droplet flames. The results show that butanol and B10 burning rates are indistinguishable from gasoline despite significant differences in sooting propensities and that gasoline and B10 droplet flames reside farther from the droplet surface than butanol droplet flames. The similar burning rates suggest the possibility that soot may not exert as strong an influence on the combustion rate as might have been expected on the basis of the thermal and chemical processes involved with soot formation. Although the data show significant deviations from the quasi-steady theory of droplet burning that neglects soot formation, scale arguments from that theory suggest that gas diffusion effects through flame temperature and liquid density are more important and consistent with the experimental trends and that soot formation may not exert as strong an influence on burning as previously conjectured for the small droplet sizes examined in this study. The results presented are also consistent with butanol being an attractive additive to gasoline to minimize consumption of gasoline (in particular) given their similar combustion rates, and reduced particulate emissions would be expected through blending based on the lower sooting propensity of butanol compared to gasoline.

#### ■ ASSOCIATED CONTENT

##### Supporting Information

Excel files that list all data displayed in Figures 7–10. This material is available free of charge via the Internet at <http://pubs.acs.org>.

#### ■ AUTHOR INFORMATION

##### Corresponding Author

\*E-mail: [cta2@cornell.edu](mailto:cta2@cornell.edu).

##### Notes

The authors declare no competing financial interest.

#### ■ ACKNOWLEDGMENTS

This work was supported by the National Aeronautics and Space Administration (NASA) under Grant NNX08AI51G with Michael Hicks as the Project Monitor. The authors also thank Zain Ali of Cornell and Prof. Yu-Cheng Liu of the University of Michigan—Flint for discussions and assistance

with some of the experiments. The assistance by Zain Ali with some of the data analyses is also appreciated. The authors also appreciate the interest of Drs. Forman Williams, Ben Shaw, Fred Dryer, and Tanvir Farouk in the work on droplet combustion.

## NOMENCLATURE

- $C_D$  = parameter related to collision integral and characteristic molecular length  
 $D$  = droplet diameter  
 $D_f$  = flame diameter  
 $D_{\text{fiber}}$  = fiber diameter (Figure 2)  
 $D_i$  = binary diffusion coefficient for gasoline ( $D_g$ ) or butanol ( $D_b$ ) in air  
 $D_s$  = soot shell diameter  
 $D_o$  = initial droplet diameter  
 $g$  = gravitation constant  
 $K$  = burning rate  
 $M_i = (W_i + W_a)/(W_i W_a)$  for gasoline ( $M_g$ ) or butanol ( $M_b$ )  
 $t$  = time  
 $T_{f,i}$  = flame temperature for gasoline ( $T_{f,g}$ ) or butanol ( $T_{f,b}$ )  
 $T_\infty$  = ambient gas temperature  
 $U_{\text{rel}}$  = relative velocity between the droplet and surrounding gas  
 $W$  = molecular weight

## Greek Letters

- $\alpha$  = gas thermal diffusivity  
 $\beta$  = gas thermal expansion coefficient  
 $\eta$  = gas kinematic viscosity  
 $\rho_i$  = gas density of gasoline ( $\rho_g$ ) or butanol ( $\rho_b$ )  
 $\rho_{L,i}$  = liquid density for gasoline ( $\rho_{L,g}$ ) or butanol ( $\rho_{L,b}$ )  
 $\nu$  = stoichiometric coefficient (Table 1)

## Subscripts

- a = air  
g = gasoline  
b = butanol  
f = flame  
i = "g" (for gasoline) or i = "b" (for butanol)

## REFERENCES

- National Research Council. *Transforming Combustion Research Through Cyberinfrastructure*; The National Academic Press: Washington, D.C., 2011; [http://www.nap.edu/openbook.php?record\\_id=13049](http://www.nap.edu/openbook.php?record_id=13049) (accessed Sept 20, 2014).
- Office of Basic Energy Sciences, Office of Science and the Vehicle Technologies Program, Office of Energy Efficiency and Renewable Energy, U.S. Department of Energy. *A Workshop To Identify Research Needs and Impacts in Predictive Simulation for Internal Combustion Engines (PreSICE)*; U.S. Department of Energy: Washington, D.C., March 3, 2011; [http://www1.eere.energy.gov/vehiclesandfuels/pdfs/presice\\_rpt.pdf](http://www1.eere.energy.gov/vehiclesandfuels/pdfs/presice_rpt.pdf) (accessed Sept 21, 2014).
- Service, R. F. *Science* **2008**, *309*, 1745.
- Ramanathan, V.; Carmichael, G. *Nat. Geosci.* **2008**, *1*, 221–227.
- Harvey, B. G.; Meylemans, H. A. *J. Chem. Technol. Biotechnol.* **2011**, *86*, 2–9.
- Jin, C.; Yao, M.; Liu, H.; Lee, C.-f. F.; Ji, J. *Renewable Sustainable Energy Rev.* **2011**, *15*, 4080–4106.
- Nigam, P. S.; Singh, A. *Prog. Energy Combust. Sci.* **2011**, *37*, 52–68.
- Wallner, T.; Miers, S. A.; McConnell, S. *J. Eng. Gas Turbines Power* **2009**, *131*, 032802.
- Durre, P. *J. Biotechnol.* **2007**, *2*, 1525–34.
- Szwaja, S.; Naber, J. D. *Fuel* **2010**, *89*, 1573–1582.
- Shapovalov, O. I.; Ashkinazi, L. A. *Russ. J. Appl. Chem.* **2008**, *81*, 2232–2236.
- Yacoub, Y.; Gautam, M.; Bata, R. *Proc. Inst. Mech. Eng., Part A* **1998**, *212*, 363–379.
- Elfasakhany, A. *Energy Convers. Manage.* **2014**, *88*, 277–283.
- Gautam, M.; Carder, D.; Martin, D. W., II *Proc. Inst. Mech. Eng., Part A* **2000**, *214*, 165–182.
- Mittal, N.; Athony, R. L.; Bansal, R.; Ramesh Kumar, C. *Alexandria Eng. J.* **2013**, *52*, 285–293.
- Costagliola, M. A.; De Simio, L.; Iannaccone, S.; Prati, M. V. *Appl. Energy* **2013**, *111*, 1162–1171.
- Zhang, Z.; Wang, T.; Jia, M.; Wei, Q.; Meng, X.; Shu, G. *Fuel* **2014**, *130*, 177–188.
- Gu, X.; Huang, Z.; Cai, J.; Gong, J.; Wu, X.; Lee, C.-f. *Fuel* **2012**, *93*, 611–617.
- Wallner, T. *J. Eng. Gas Turbines Power* **2011**, *133*, 082801.
- Schulz, M.; Clark, S. *J. ASTM Int.* **2011**, *8*, JAI103068.
- Merola, S. S.; Valentino, G.; Tornatore, C.; Marchitto, L. *Energy* **2013**, *62*, 150–161.
- Merola, S.; Tornatore, C.; Marchitto, L.; Valentino, G.; Corcione, F. *Int. J. Energy Environ. Eng.* **2012**, *3*, 6.
- Dernotte, J.; Mounaim-Rousselle, C.; Halter, F.; Seers, P. *Oil Gas Sci. Technol.* **2009**, *65*, 345–351.
- Alasfour, F. N. *Appl. Therm. Eng.* **1997**, *17*, 537–549.
- Alasfour, F. N. *Int. J. Energy Res.* **1997**, *21*, 21–30.
- Deng, B.; Fu, J.; Zhang, D.; Yang, J.; Feng, R.; Liu, J.; Li, K.; Liu, X. *Energy* **2013**, *60*, 230–241.
- Feng, R.; Yang, J.; Zhang, D.; Deng, B.; Fu, J.; Liu, J.; Liu, X. *Energy Convers. Manage.* **2013**, *74*, 192–200.
- Zhang, Y.; Boehman, A. L. *Combust. Flame* **2010**, *157*, 1816–1824.
- Tornatore, C.; Marchitto, L.; Valentino, G.; Esposito Corcione, F.; Merola, S. S. *Energy* **2012**, *45*, 277–287.
- Venugopal, T.; Ramesh, A. *Appl. Therm. Eng.* **2013**, *59*, 550–558.
- He, B.-Q.; Liu, M.-B.; Yuan, J.; Zhao, H. *Fuel* **2013**, *108*, 668–674.
- Yang, B.; Yao, M.; Cheng, W. K.; Zheng, Z.; Yue, L. *Fuel* **2014**, *120*, 163–170.
- Venugopal, T.; Ramesh, A. *Int. J. Energy Res.* **2014**, *38*, 1060–1074.
- Venugopal, T.; Ramesh, A. *Fuel* **2014**, *115*, 295–305.
- Sarathy, S. M.; Oßwald, P.; Hansen, N.; Kohse-Höinghaus, K. *Prog. Energy Combust. Sci.* **2014**, *44*, 40–102.
- Cai, J.; Zhang, L.; Zhang, F.; Wang, Z.; Cheng, Z.; Yuan, W.; Qi, F. *Energy Fuels* **2012**, *26*, 5550–5568.
- Rosado-Reyes, C. M.; Tsang, W. *J. Phys. Chem. A* **2012**, *116*, 9825–9831.
- Vasu, S. S.; Sarathy, S. M. *Energy Fuels* **2013**, *27*, 7072–7080.
- Grana, R.; Frassoldati, A.; Faravelli, T.; Niemann, U.; Ranzi, E.; Seiser, R.; Cattolica, R.; Seshadri, K. *Combust. Flame* **2010**, *157*, 2137–2154.
- Agathou, M. S.; Kyritsis, D. C. *Appl. Energy* **2012**, *93*, 296–304.
- Dagaut, P.; Sarathy, S. M.; Thomson, M. J. *Proc. Combust. Inst.* **2009**, *32*, 229–237.
- Kadota, T.; Mizutani, S.; Wu, C.-Y.; Hoshino, M. Fuel droplet size measurements in the combustion chamber of a motored SI engine via laser Mie scattering. *SAE Tech. Pap. Ser.* **1990**, DOI: 10.4271/900477.
- Tabata, M.; Nagao, A.; Iida, Y. *Int. Sym. COMODIA* **1990**, 179–184.
- Maricq, M. M.; Podsiadlik, D. H.; Brehob, D. D.; Haghgooe, M. Particulate emissions from a direct-injection spark-ignition (DISI) engine. *SAE Tech. Pap. Ser.* **1999**, DOI: 10.4271/1999-01-1530.
- Zhao, F.; Lai, M.-C.; Harrington, D. L. *Prog. Energy Combust. Sci.* **1999**, *25*, 437–562.
- Sirignano, W. A. *Dynamics and Transport of Droplets and Sprays*; Cambridge University Press: Cambridge, U.K., 1999; pp 10–21.

- (47) Alam, F. E.; Liu, Y. C.; Avedisian, C. T.; Dryer, F. L.; Farouk, T. *I. Proc. Combust. Inst.* **2015**, *35*, 1693–1700.
- (48) Farouk, T. I.; Dryer, F. L. *Combust. Flame* **2012**, *159*, 3208–3223.
- (49) Jackson, G. S.; Avedisian, C. T.; Yang, J. C. *Int. J. Heat Mass Transfer* **1992**, *35*, 2017–2033.
- (50) Bartle, K. D.; Fitzpatrick, E. M.; Jones, J. M.; Kubacki, M. L.; Plant, R.; Pourkashanian, M.; Ross, A. B.; Williams, A. *Fuel* **2011**, *90*, 1113–1119.
- (51) Hoxie, A.; Schoo, R.; Braden, J. *Fuel* **2014**, *120*, 22–29.
- (52) Jangi, M.; Sakurai, S.; Ogami, Y.; Kobayashi, H. *Combust. Flame* **2009**, *156*, 99–105.
- (53) Ogami, Y.; Sakurai, S.; Hasegawa, S.; Jangi, M.; Nakamura, H.; Yoshinaga, K.; Kobayashi, H. *Proc. Combust. Inst.* **2009**, *32*, 2171–2178.
- (54) Wu, H.; Nithyanandan, K.; Lee, T. H.; Lee, C.-f. F.; Zhang, C. *Energy Fuels* **2014**, *28*, 6380–6391.
- (55) Liu, Y. C.; Avedisian, C. T. *Combust. Flame* **2012**, *159*, 770–783.
- (56) Nakaya, S.; Fujishima, K.; Tsue, M.; Kono, M.; Segawa, D. *Proc. Combust. Inst.* **2013**, *34*, 1601–1608.
- (57) Liu, Y. C.; Xu, Y.; Avedisian, C. T.; Hicks, M. C. *Proc. Combust. Inst.* **2015**, *35*, 1709–1716.
- (58) Avedisian, C. T.; Callahan, B. J. *Proc. Combust. Inst.* **2000**, *28*, 991–997.
- (59) Shaw, B. D.; Chen, A. G. *Microgravity Sci. Technol.* **1997**, *10*, 136–143.
- (60) Dembia, C. L.; Liu, Y. C.; Avedisian, C. T. *Image Anal. Stereol.* **2012**, *31*, 137–148.
- (61) Jackson, G. S.; Avedisian, C. T. *Combust. Sci. Technol.* **1996**, *115*, 125–149.
- (62) Turns, S. R. *An Introduction to Combustion*, 3rd ed.; McGraw-Hill: New York, 2012; pp 396 and 702.
- (63) Farouk, T. I.; Liu, Y. C.; Savas, A. J.; Avedisian, C. T.; Dryer, F. L. *Proc. Combust. Inst.* **2013**, *34*, 1609–1616.
- (64) Jackson, G. S.; Avedisian, C. T. *Proc. R. Soc. London, Ser. A* **1994**, *446*, 255–276.
- (65) Nayagam, V.; Marchese, A.; Sacksteder, K. Microgravity droplet combustion: An inverse scale modeling problem. In *Progress in Scale Modeling*; Saito, K., Ed.; Springer: Dordrecht, Netherlands, 2008; pp 169–178.
- (66) Reid, R. C.; Prausnitz, J. M.; Poling, B. E. *The Properties of Gases and Liquids*, 4th ed.; McGraw-Hill: New York, 1987; pp 581–582 and 688.
- (67) Aharon, I.; Shaw, B. D. *Microgravity Sci. Technol.* **1997**, *10*, 75–85.
- (68) Andersen, V. F.; Anderson, J. E.; Wallington, T. J.; Mueller, S. A.; Nielsen, O. J. *Energy Fuels* **2010**, *24*, 2683–2691.
- (69) Yanowitz, J.; Christensen, E.; McCormick, R. L. *Utilization of Renewable Oxygenates as Gasoline Blending Components*; National Renewable Energy Laboratory (NREL): Golden, CO, 2011; NREL/TP-5400-50791, <http://www.nrel.gov/docs/fy11osti/50791.pdf> (accessed Sept 19, 2014).
- (70) Christensen, E.; Yanowitz, J.; Ratcliff, M.; McCormick, R. L. *Energy Fuels* **2011**, *25*, 4723–4733.